Three-dimensional reconstruction of neovasculature in solid tumors and basement membrane matrix using ex vivo X-ray micro-computed tomography

Seunghyung Lee[1,2], **Mary F. Barbe**[1], **Rosario Scalia**[3], and **Lawrence E. Goldfinger**[1,2,4]

[1]Department of Anatomy & Cell Biology, Temple University School of Medicine

[2]The Sol Sherry Thrombosis Research Center, Temple University School of Medicine

[3]Department of Physiology and the Cardiovascular Research Center, Temple University School of Medicine

[4]Cancer Biology Program, Fox Chase Cancer Center, Philadelphia, PA 19140

Abstract

Objective—To create accurate, high resolution 3D reconstructions of neovasculature structures in xenografted tumors and Matrigel plugs for quantitative analyses in angiogenesis studies in animal models.

Methods—The competent neovasculature within xenografted solid tumors or Matrigel plugs in mice was perfused with Microfil, a radio-opaque, hydrophilic polymerizing contrast agent, by systemic perfusion of the blood circulation via the heart. The perfused tumors and plugs were resected and scanned by X-ray micro-computed tomography to generate stacks of 2D images showing the radio-opaque material. A non-biased, precise post-processing scheme was employed to eliminate background X-ray absorbance from the extra-vascular tissue. The revised binary image stacks were compiled to reveal the Microfil-casted neovasculature as 3D reconstructions. Vascular structural parameters were calculated from the refined 3D reconstructions using the scanner software.

Results—Clarified 3D reconstructions were sufficiently precise to allow measurements of vascular architecture to a diametric limit of resolution of 3 μm in tumors and plugs.

Conclusions—*Ex vivo* micro-computed tomography can be used for 3D reconstruction and quantitative analysis of neovasculature including microcirculation in solid tumors and Matrigel plugs. This method can be generally applied for reconstructing and measuring vascular structures in 3 dimensions.

Keywords

Micro-computed tomography (microCT); Vascular imaging; Tumor angiogenesis; Matrigel plug; Microvasculature

Correspondence should be addressed to: Lawrence Goldfinger - goldfinger@temple.edu, phone: 215.707.8157, fax: 215.707.6499.

INTRODUCTION

Many imaging modalities exist for visualizing angiogenic responses in animal models [8, 9, 10]. A cohort of newer techniques such as contrast-enhanced MRI, marker-based intravital microscopy coupled with optical frequency domain imaging, and both *in vivo* and *ex vivo* X-ray micro-computed tomography (microCT/μCT) have emerged with the promise of providing 3D structural information that previously was inaccessible by standard 2D imaging analysis. A major goal in the development of these techniques is the ability to achieve sufficiently high resolution to visualize the microcirculation [15, 30]. Recent studies have used μCT to quantify the number of small vessels in lung tumors and to generate 3D vascular reconstructions in other systems [12, 16, 35, 36]. However, a persistent problem is the precise elimination of background absorbance from the scans, which precludes accurate reconstruction and measurements of the vascular structures [10]. We have modified the scanning and image processing to reconstruct and measure neovascular structures including small vessels in carcinomas and melanomas in a knockout mouse model [24].

Neovasculature in tumors is believed to have unique structural properties, reflecting unique functional properties. Blood vessels in tumors are more dynamic, tortuous and permeable, and perfuse poorly, compared to their normal counterparts in non-pathological settings. Furthermore, the microcirculation in tumors can be heterogeneous and does not resemble the usual hierarchy of arterioles, capillaries and venules [3, 11, 19, 22]. Thus, the ability to reconstruct and measure the structure of neovasculature in tumors and other settings is key to understanding the biological basis for these effects, and to develop targeting strategies [5, 9, 10, 14, 15].

Although a variety of *in vivo* and *ex vivo* platforms other than solid tumor models for analyzing angiogenesis exist, sub-cutaneous (s.c.) implantation of basement membrane matrices such as Matrigel as a tissue-free receptacle for neovascularization has remained a widely used tool, due in part to its ease of use [32]. Matrigel is a partially defined extract from the Engleberth-Holm Swarm tumor, consisting of basement membrane proteins and several growth factors [2, 41]. Matrigel from which low molecular mass proteins such as growth factors have been extracted by ammonium sulfate treatment ("growth factor-reduced" Matrigel) is commonly used as a substrate for co-mixing of defined factors such as vascular endothelial growth factor (VEGF) or basic fibroblast growth factor prior to implantation [28, 39]. The resulting invasion of endothelial cells from the host animal and subsequent formation of endothelial networks within the Matrigel plugs models angiogenic capillary network formation - albeit in an isolated, tissue-free environment - which is commonly assessed by histological examination of 2D sections from the resected plugs [2, 32]. However, this method has eluded standardization, due to heterogeneity of the plug size and composition, as well as sampling variability from 2D sectioning [28, 32]. Hence, analysis of *ex vivo* angiogenic platforms such as Matrigel plugs, like solid tumor models, would also benefit from 3D vascular reconstruction.

In this study we have refined a μCT-based technique for 3D reconstruction and quantitative analysis of neovasculature in xenografted tumors as well as Matrigel plugs in mice. An

isotropic voxel limit of resolution of 3 μm, coupled with thorough depletion of background absorbance using a precise, non-biased image processing scheme, allows for accurate quantitation of vascular architectural parameters, including the microvasculature. We propose that this system will be generally applicable for testing angiogenic responses *ex vivo*.

MATERIALS AND METHODS

Mice

24 C57BL/6 mice between the ages of 6 and 8 weeks were used for all experiments. For surgical procedures, ketamine-HCl (40 mg/kg) and xylazine (10 mg/kg) (Ketaset) were administered by intraperitoneal injection as anesthetic prior to surgery. All animal experiments followed protocols approved by the Institutional Animal Care and Use Committee (IACUC) at Temple University.

Cell culture and inoculation of tumor cells *in vivo*

Lewis lung carcinoma (LL/2, LLC) cells were obtained from American Type Culture Collection (Rockville, MD). The cells were cultured in DMEM with 10% FBS in a humidified, 5% CO_2 atmosphere at 37°C. LLC cells were harvested by trypsinization, washed and resuspended at 1×10^6 cells/500 μL of DMEM without serum, and this suspension was injected subcutaneously into the flank of 6–8-week-old C57BL/6 mice. The peripheral circulation was perfused with Microfil and mice were euthanized within 10 d post-injection.

Angiogenesis in Matrigel plugs

The angiogenesis model was based on the use of Matrigel (BD Biosciences) implants in C57BL/6 mice. 500 μL growth factor-reduced Matrigel with or without 100 ng/mL of VEGF was injected s.c. in the mouse flank. After 3, 7, or 10 days the plugs were perfused with Microfil as described below, mice were euthanized and the Matrigel plugs were dissected away from the tissue, photographed, and then fixed with 10% formalin/PBS for 48 hours at room temperature prior to scanning.

Vascular perfusion with Microfil

A freshly prepared solution of Microfil compound (MV-120, Flow Tech, Inc.) was prepared and used immediately, according to the manufacturer recommendations. We used a blue version of Microfil although other colors are also available. It consisted of 42% of MV-120, 53% of the diluent solution and 5% of a curing agent. The abdominal cavity and rib cage of each plug- or tumor-bearing mouse was opened under anesthesia. Intracardial cannulation of the left ventricle was done with a 27 ½ g. needle connected to a polyethylene catheter with 1.6 mm tubing while simultaneously nicking the right atrium, and the mouse circulation was perfused with 20 mL of a 0.1% heparinized solution in phosphate-buffered saline (heparin; Sigma, H3393) through a pressurized pump (Masterflex System Model 7553-70, Cole Palmer) at 2 mL/min, which we found was sufficient for optimal perfusion but did not result in vascular damage. Thereafter, 20 mL of the Microfil mixture was perfused through the same catheter by stopping the pump, moving the back end of the catheter tubing to a 50-mL

conical tube containing fresh Microfil solution, and then re-starting the pump [16]. Perfusion was allowed to continue for 20 minutes, during which procedure the animal dies under anesthesia. Obvious perfusion in the eyes and tail served as a reliable marker for systemic perfusion of the blood circulation. The neovasculature was also obviously perfused in the LLC tumors and Matrigel plugs (as indicated by blue colored vessels in the tumor and plugs, post-perfusion.) The Microfil solution was allowed to polymerize at 4°C overnight, after which the tumors or plugs were resected with surgical scissors, and fixed overnight in 10% formalin/PBS.

Scanning

Fixed samples were scanned in a μCT system [6]. A Skyscan 1172, 11 MPixel camera model, high resolution cone-beam μCT scanner (Skyscan, Ltd, Antwerp, Belgium) was used. The specimens were placed inside a 13 mm-diameter ultracentrifuge tube (Nalgene, 3410–1351) with the bottom cut off and replaced with a plug of poster putty for placement on the scanner stage. Multiple specimens can be layered within the tube so long as they do not overlap across the horizontal. It is essential to avoid encasing the specimens in wrapping, such as Parafilm, as the wrapping material may absorb X-rays and be visible in the scanned images, which will complicate 3D reconstruction later. The top of the tube was plugged with poster putty to prevent dehydration of the specimens during scanning. The tube was positioned vertically onto the computer-controlled rotation stage of the μCT system. MicroCT scanning and analysis was performed according to recent guidelines [6]. The following settings were used: camera pixel size of 8.75 μm (*i.e.*, the near setting for the camera), image pixel size of 3 μm, source voltage of 60 kV, source current of 130 μA, no filter, frame averaging of 4, and scanned 180° around the vertical axis in rotation steps of 0.28°, one specimen per scan. The average scan duration was 1 hour. These slices were reconstructed into 3D reconstructions using cone-beam reconstruction software (Skyscan NRecon) based on the Feldkamp algorithm, a process that yielded a total of ~ 3500 image slices per sample that were 3.0 μm thick in the axial plane. The following reconstruction settings were used: a ring artifact correction of 12, a beam hardening correction of 20%, no smoothing, and a post-alignment correct of 1.

Summary of 3D reconstruction, image processing and 3D analysis

The 3D construction and image processing were performed using the SkyScan accompanying software: NRecon, CTAn and CTVox [29]. First, the images were resized by ¼, since reconstructed files were very large, which greatly slowed the computer processing. Second, the resized whole image was selected as a region of interest (ROI), and then saved as a new series of image files. Next the ROI image series was reloaded onto CTAn. The ROI images were processed from the 2D stack to create a stack of binary images and to eliminate background pixels (voxels in 3D.) Once the 2D stack was refined, CTAn 3D analysis was performed to obtain vessel volumes and surface areas. Analyze 10.0 (AnalyzeDirect) was used to generate tree maps and to measure branch angles and segment lengths.

3D reconstruction with CTVox

1. Reconstruct by SkyScan's volumetric reconstruction software, NRecon:

2. Open NRecon for 3D reconstruction with scanned files.

3. Select the scanned image top and bottom, and then "preview" to make sure the entire specimen is contained in the file series.

4. Set output ranges from 0.0 to 0.1, choose a unique destination folder, and save as a series of 8-bit BMP (bitmap image file format) image files in the new folder.

5. Start the 3D reconstruction (typically overnight.)

6. Open the reconstructed files within the CTVox program.

7. Set up Log-Scale histogram on the channel screen.

8. Slide the histogram bar line to highlight the vessels and deplete the extravascular material from the image, and then save the 3D reconstruction as a single 2D image, as a 3D CTVox image (large file) or as a rotating movie of the 3D reconstruction using the flight recorder.

3D reconstruction analysis from compiled 2D stacks

1. Open the CTAn program and open the reconstructed files. Optional: resize the files to ¼ of the original size. This step greatly reduces computer processing time for large (~1 cm^3) samples. The reconstructions do not need to be resampled to the original size prior to analysis, as CTAn converts the sample dimensions during the "resize" step. We compared resized (both ¼ and ½ size) to non-resized images followed through the remaining steps, and found the reconstructions and subsequent analysis to yield identical results (not shown.)

2. Select Regions of interest (ROI) by widening an ROI circle around the area including the specimen, but excluding the outer tube. The tube can be seen as a thick circle around the periphery in each image. Although it is not strictly necessary, a tighter fitting volume of interest (VOI) can be created by resizing the ROI at multiple image slices within the stack. This will "crop" the VOI and can reduce processing time for the thresholding and despeckling steps later.

3. Save the selected ROI to a new folder as "voi.ROI".

4. Open the ROI files. (See example in Figure 2B.)

5. Set up and run the following Task list:

   a. Thresholding: Mode, Global; Lower grey threshold, 30; Upper grey threshold, 255. (See example in Figure 2C.)

   b. Despeckle: remove white speckles/3D space/less than 100 voxels/apply to image. (See example in Figure 2D.)

   c. Thresholding: Mode, Global; Lower grey threshold, 75; Upper grey threshold, 255. (See example in Figure 2E.)

   Processing at this step can take several hours. The final result will be a series of background-subtracted binarised 2D images with solid white "vessel" sections against a black background. Reconstructions can be

visualized using various software packages, such as CTVox or CTVol accompanying software (Figure 3A.)

6. Check processed images by reopening the "voi.ROI" files, and then chose the Task for "3D analysis."

7. Select "Preferences", set units to μm, and then run the "3D analysis" Task.

8. Copy the outputs to a database program such as Microsoft Excel.

9. Tree analysis, as in Figure 4, can also be carried out with the completed reconstructions using Analyze (AnalyzeDirect). In our studies, we used Microsoft Excel to compile data from the tree analysis and Kaleidograph to generate dot and box plots.

10. Tortuosity (Tg) was calculated using a surface-based distance metric (Phil Salmon, Bruker-microCT, personal communication.) Surface areas (SSA), thickness (vessel diameter, D), and volumes (V) were derived from CTAn as described above. Like the Distance Metric [7], general tortuosity can be determined as the ratio of surface areas of given vessels to the surface areas of idealized cylinders with the same volume and diameters [1]. Surface area of a cylinder (length × circumference) can be expressed as $(4 \times V)/D$. Hence, we used the following calculation for general tortuosity: $Tg = (SSA \times D)/(4 \times V)$.

Statistical analysis

One-way ANOVA followed by Fisher PLSD analysis was used for all statistical data analysis, using StatView (SAS). A 5% probability was considered significant.

RESULTS

Using Microfil perfusion, μCT scanning, and 3D reconstruction of tumor vasculature, we recently determined that angiogenesis in xenografted tumors in mice deleted for the RLIP76 gene was substantially blocked compared to wild type (WT) [24]. The neovasculature was analyzed days to weeks later, after angiogenesis in the xenografts has occurred. This method relies on the perfusion of competent vessels connected to the peripheral circulation within the tumor, with the hydrophilic, silicon-based polymerizing contrast agent Microfil, perfused via a catheter inserted in the heart [16]. Based on these initial results, we sought to refine this method further to be useful as a general tool for *ex vivo* angiogenesis or other vascular studies.

We optimized the perfusion, μCT scanning and image processing steps to generate 3D reconstructions of the neovasculature in the resected tumors, with an isotropic voxel size of 3 μm (Figures 1, 2), ensuring inclusion of narrow vessels (capillaries) and minimal background in the reconstructions [24]. We applied this revised method for observing the development of neovascular structures in developing solid tumors in mice over time *ex vivo*. Microfil was perfused at a steady flow rate at 2 mL/min through the left ventricle via a catheter attached to a perfusion pump (Figure 1A and B), in C57Bl/6 mice 7 and 10 d after bolus injection of LLC cells. The dark blue Microfil suspension perfused the peripheral

circulation quickly, as within seconds, blood vessels could clearly be seen to fill with the blue Microfil throughout peripheral tissues, including the spleen, colon and other organs (Figure 1C), and upon later inspection, blood vessels in the brain were also perfused (results not shown.) By 7 d and later at 10 d, discrete solid neoplasias had formed, and these were deeply perfused with the Microfil solution, which included small diameter vessels (Figure 3A.) Tumor volumes at 7 d and 10 d averaged 466 and 568 mm^3, respectively. Gross examination indicated little, if any, leakage of the Microfil from the blood circulation into the surrounding tissue (Figure 1D), indicating that in this system, perfusion did not rupture most vessels, and the perfused vessels were impermeable to the compound, which is a large polymer.

We next imaged the neovasculature by μCT scanning of the Microfil-perfused, resected tumors at 3 μm isotropic voxel resolution, using a Skyscan μCT scanner (Figure 2A; see **Materials and Methods**) (SkyScan, Kontich, Belgium). The scanner created a stack of 2D images that could then be compiled into a 3D reconstruction. However, in order to reconstruct the Microfil-perfused vasculature accurately – particularly the microvasculature - it was essential to eliminate the background X-ray absorbance, representing the surrounding tumor tissue as well as the tube in which the samples were placed, from the 2D images before 3D compiling (Figure 2B), while simultaneously preserving the regions of the image which represented the Microfil vascular casts in each image. Therefore we developed a simple yet precise, non-biased, threshold-based image-processing scheme using the accompanying software to apply to the image stacks, which yielded a stack of 2D binary images for each sample representing only the radio-opaque regions, corresponding to the perfused vessels (Figure 2E and F; see **Materials and Methods**.) An initial threshold step with a lower grey value of 30 (using a 1–255 LUT) was determined empirically, using 30 randomly selected fields, to be the minimum level to reduce background tissue absorbance to be low enough for subtraction in subsequent steps, while maintaining pixels (representing voxels) derived from Microfil X-ray absorbance (cf. Figure 2B and C.) Next, the despeckle function was applied in 3D to subtract background absorbance voxels; again the minimal voxel size (100) was determined empirically to eliminate non-vessel voxels, well below a threshold for microvessels, for which even the shortest vessels corresponded to several hundred voxels (Figure 2D.) Finally, a second threshold was applied with a slightly higher minimum grey value, which we determined resulted in nearly complete elimination of spurious absorbance pixels without altering or deleting pixels derived from vessel casts (Figure 2E). Manual inspection of the raw and processed image stacks confirmed that the processing scheme selectively preserved the Microfil absorbance, including small voxels representing the microvasculature, and effectively deleted the background material (Figure 2B–F.)

From the scans we generated 3D reconstructions of the neovasculature as binarised images that included small vessels and minimal background voxels (Figure 3A, top row.) Skeletonized images can also be generated from these reconstructions (Figure 3A, bottom row.) We also generated movies to visualize the 3D reconstructions in full rotation (Supplementary Movies 1, 2.) These reconstructions not only offered new views of the tumor vasculature, but allowed us to measure the vascular geometries, including total and

individual vessel volumes, and individual vessel diameters at the widest points (presumed to be the branch points.) Measurements of total vessel volumes of each structure complemented visual inspection of the reconstructions and confirmed the progressive neovascularization in the developing tumors (Figure 3B and Table 1.) From the 3D reconstructions we also calculated individual vessel diameters and volumes. Figure 3C shows the range of vessel diameters as a frequency function of the total vascular volumes at 7 d and 10 d, and Figure 3D shows the distribution of vessel volumes as a function of vessel diameters. These reconstructions included vessels with diameters in the range of 3–14 μm, indicating capillaries, and volumes of these individual small vessels could be calculated. By 10 d there was a broader distribution of vessel volumes, thicknesses, and by extension, vessel lengths in the tumors. Vascular specific surface area (SSA, Figure 3E) and micro-vascular density (MVD, Figure 3F) determinations showed a trend toward increased SSA and MVD in the 10 d tumors (although these differences were not significant), confirming the volume and diameter measurements and indicating an increase in abundance of smaller vessels in the 10 d tumors (see also Table 1.)

The apparently high connectivity in the reconstructions allowed us to convert the 3D images into segmented tree structures for further analysis of the vascular architecture including segment length and branching structure. Representative analysis is shown in Figure 4. Each new branch in the tree map (Figure 4A) represented either a side branch or bifurcation from the parent vessel. Branch angles in both the 7 d and 10 d reconstructions showed a broad distribution with a nearly identical median, demonstrating no significant median difference in branch angles at the two time points (Figure 4B and Table 1.) Segment lengths also varied greatly in tumors at both 7 d and 10 d; however, the median segment lengths were identical (Figure 4C and Table 1.) The segment length measurements represent distances between branches or bifurcations; thus, there was no difference in the overall distribution of vessel branching in the more mature tumors. However, these analyses revealed several differences in vascular architecture in the 7 d and 10 d tumors, as implicated by vessel volume and diameter measurements (Figure 3). As shown in Figure 4B, branch angle measurements of 0° (empty columns along the abscissa) indicate vessels with no branches or bifurcations. Notably, there was a higher concentration of non-branched vessels furthest from the root in the 7 d tumors than in the 10 d tumors (right side of the histograms), indicating extensive branching throughout the larger vascular tree in the more mature tumors. Similarly, as shown in Figure 4C, whereas the median length and overall distribution of segments was the same between these tumors, there was a ~30% increase in the total number of segments at 10d compared to 7 d, confirming the presence of longer vessels (*i.e.*, more segments, given a similar distribution of branches). The longer vessels also correlated with an overall increase in tortuosity. Ratios of vessel length to the minimal linear distance between endpoints (*e.g.*, of cylinders) rose from 1.25 ± 0.31 at 7 d, to 2.63 ± 0.67 at 10 d, indicating an increase in vascular curvature over time in the tumors (Table 1; see **Materials and Methods**). Together, these metrics corroborate the reconstructions showing a more extensive tree structure at 10 d.

We next extended the 3D vascular reconstruction approach to analyze neovasculature in Matrigel plugs in the absence of tumor cells. We used growth factor-reduced Matrigel plugs

(500 mm^3) ± 100 ng/mL VEGF, injected into the mouse flanks, and perfused with Microfil at 3, 7, or 10 d for μCT scanning. The plugs showed progressive neovascularization over time, with or without VEGF, based on the presence of Microfil and apparent enrichment of the plugs with blood. Thus, Matrigel plugs support infiltration of competent vessels which can be perfused from the peripheral circulation. Gross observations of the Microfil-perfused plugs, facilitated by the translucency of the plugs and opacity of the Microfil, suggested that most of the neovasculature was localized to the periphery of the plugs, even after 10 d (Figure 5A.) Plugs scanned at 3 d showed no apparent X-ray absorbance over background, indicating that substantial angiogenesis did not occur until at least 3 d after implantation (results not shown.) However, we were able to generate 3D vascular reconstructions as early as 7 d after implantation, as well as in 10 d plugs. We then scanned the plugs by μCT and generated 3D reconstructions using the same parameters as for the resected tumors (Figure 5B.) The 3D reconstructions recreated "vessels" which closely resembled the overall appearance of the perfused plugs (cf. Figure 5A and B), indicating that the same scanning and reconstruction parameters used for tumors will also reproduce accurate 3D vascular reconstructions from Matrigel plugs. From these we calculated vessel volumes (Figure 5C) and vessel diameters measured at the widest points (Figure 5D, E.) These parameters corroborated the visual inspection, such that total vessel volumes increased over time (Figure 5C), with larger diameter vessels appearing later (Figure 5D, E), indicating vessel maturation. As expected, the addition of VEGF was associated with an increase in all of these parameters. Thus, new blood vessel formation in Matrigel plugs can be monitored dynamically by μCT scanning, 3D reconstruction, and quantitative analysis.

DISCUSSION

We have refined a generalizable method of *ex vivo* X-ray μCT scanning and computer-assisted 3D reconstruction of Microfil-perfused vascular structures, including microvasculature, which can be applied to studying formation and topological features of neovasculature in normal and pathological angiogenesis in animal models. The 3 μm resolution lower limit of the scans (lower than the 15–16 μm isotropic voxel size from several previous studies [12, 16, 36]) ensured inclusion of the capillary structures within the 3D reconstructions. Importantly, thorough depletion of background absorbance using a precise, non-biased, threshold-based image processing scheme (see **Materials and Methods**) allowed for accurate reconstruction and subsequent quantitation of vascular volumes, diameters, branch angles, segment lengths, and other morphological parameters from the resultant 3D reconstructions which included microvasculature [12].

This system offers more thorough structural characterization of vasculature than 2D image analysis such as in histological sections and several other intravital imaging methods, in roughly the same amount of analysis time [9, 14]. The time for the overall procedure (starting with the day of perfusion, *i.e.*, after angiogenesis has been induced) can range from a few days up to one week, depending on several factors, including the size of each specimen, the perfusion efficiency, and the processing speed of the computer running the software. μCT scanning can be left to run overnight, and using our scanning parameters, takes approximately 3–4 hr for a sample diameter of ~ 1 cm. Up to three samples can be placed in the scanner for a single (partitioned) scanning procedure which can be run

overnight. 3D reconstruction, which occurs after the scanning step, can also be run overnight, but must be run separately for each specimen and takes ~ 3 hours per specimen. Post-reconstruction quantitative analysis can be completed within a few hours.

Perfusion with Microfil relies on the competency of the vessels within the structure of interest. Thus, we have also confirmed that vessels in Matrigel plus can be perfused, resulting in accurate vascular casting in the plugs [17, 34]. The apparent restriction of the neovasculature to the plug peripheries may reflect angiogenesis initiating from multiple points in the host vasculature and invading the plug from many directions, in contrast to the more tree-like structures in the tumors. Alternatively, "dead end" vessels could represent sealed or damaged vessels, or could also reflect limited perfusion due to localized fluctuations in perfusion pressure. Similarly, tumor vessels with low patency may be missed with μCT casting approaches.

μCT cast analysis does not rely on expression of specific vascular cell markers (*e.g.*, CD31 or smooth muscle actin), on the selectivity of marker expression under particular conditions, or on the ability of tracer probes to access those markers by any labeling methods. However, radio-opaque tracers designed to absorb X-rays are conceivable [8, 10, 19, 33]. We have found that using the heart catheter, the Microfil compound readily perfused and formed a cast of the complete blood circulation, including within the brain (not shown), and perfusion was rapid in mice. These results suggest that this method may also be applicable to studies in larger animal models, without the Microfil hardening too quickly. It should be noted that contrast agents such as Microfil in vascular reconstructions may not be as useful in more advanced tumors, or in other model systems in which vessel permeability may be high and the agent can leak through weak and damaged parts of the vessel wall [22]. However, Microfil is a large polymer and may not be useful by itself for assaying vascular permeability, although it has been combined with other contrast agents for this purpose [23].

Accurate 3D reconstructions of neovascular structures derived by this method can be used to assess multiple morphological features with implications for the unique properties of the vasculature in pathological settings. For example, tumor neovasculature is believed to be more tortuous and less hierarchically organized than normal blood vessels, and we have found that tortuosity increased in the tumor vasculature over time in the carcinoma xenografts. Our results closely match those found in gliomas [7]. Other morphological measurements, including branch angles and segment lengths, provide an indication of the distribution of vessels in the tree structure and also can indicate hemodynamic properties [3, 5, 11, 19, 25, 26, 38]. In our reconstructions of tumor neovasculature in Lewis lung carcinoma xenografts in mouse flanks, we found a broad distribution of branch angles but a narrow distribution of segment lengths between branch points throughout the tree structure, with no distinct changes in patterns of segment length across vessel generations from the root to the tips of the tree (Figure 4.) These findings are in contrast to previous studies using maceration casts and other modeling techniques in other tumor models in mice, which showed increasing branch order (*i.e.*, shorter segment lengths) at higher generations, variability in lengths that did not seem to correspond hierarchically, and other unusual properties such as loop structures or long non-branched segments; however, in our studies vessel diameters did vary widely, particularly at 10 d, as in previous studies [26, 31, 37].

The particular vascular architecture in the xenografts in this study may reflect heterogeneity in neovascular tree structure depending on the tumor type; for example, in our previous studies with this method we observed that neovascular trees in xenografted B16 melanomas consisted primarily of a single axial artery interspersed with small-diameter, relatively straight lateral branches, as opposed to the evidently more tortuous architecture of the LLC tumor vasculature [24]. The basic structure of sprouting from a large axial vessel appears to be a common feature of tumor neovasculature [13]. However, a relatively small range of examples of μCT 3D reconstructions of tumor neovasculature have been reported to date, making broad, direct comparisons with other modeling or reconstruction efforts difficult. As 3D reconstructions or models of tumor vasculature continue to be examined, more thorough characterization of the distinctive nature of tumor angiogenesis may emerge.

Vascular parameters such as vascular network flow pathways, hemodynamics, and the distribution and morphologies or other properties of cells of the vessel wall cannot be determined directly with this method, as the vascular tree reconstructions are generated from casts of the patent vessel lumens. For example, tumor vessels cannot be assumed to be cylindrical – which has direct implications for hemodynamic properties [13] – but this level of architectural detail was not evident in branch point diameter measurements. However, SSA and MVD determinations provide surrogate indications of overall transport capacity of the vasculature, and here we find SSA in LLC tumors comparable to previously reported levels for colonic carcinoma xenografts, suggesting a similar degree of vessel caliber in the Lewis lung carcinoma xenografts [13]. MVD levels were also within a similar range to other carcinoma xenografts [13]. MVD, based on intervessel distance, is determined by the balance of local angiogenic and anti-angiogenic factors, as well as by other factors such as local nutrient concentrations; thus, our results suggest an increase in both angiogenesis as well as metabolic burden of the tumor cells [18]. Furthermore, coupling hemodynamic assessments such as by dynamic contrast-enhanced MRI or CT [11, 21, 27] with μCT-based tree reconstruction, can be explored in animal models as a way to determine flow variability within the tumor neovasculature (e.g., tissue blood flow, blood volume, mean transit time, and capillary permeability) as functions of the tree architecture [4, 20]. Hence, each of these imaging and modeling approaches, including cast reconstructions such as in this study, is alone insufficient to yield the complete spectrum of vascular parameters, but combinatorial approaches as well as continual refinement of these methods can improve imaging and subsequent analysis further. Another obvious drawback to the method is that it is invasive, and the animal subjects have to be sacrificed in order to perform the experiments. Thus, one animal must be used for each time point or other variable. The structure of interest must be able to be accommodated by the scanner; in our case the specimen size limit was 50 mm in height, width and length [24, 40]. This method also could conceivably be used to evaluate vasculogenesis and to map vascular structures in developed organs and soft tissues. Finally, this method cannot be used for human subjects as it is an *ex vivo* μCT technique.

Supplementary Material

Refer to Web version on PubMed Central for supplementary material.

Acknowledgments

Abbreviations

DMEM	Dulbecco's Modified Eagle Medium
FBS	Fetal bovine serum
LLC	Lewis Lung carcinoma
μCT	micro-CT, micro-computed tomography
PBS	phosphate-buffered saline
ROI	region of interest
VEGF	vascular endothelial growth factor
VOI	volume of interest

References

1. Azegrouz H, Trucco E, Dhillon B, MacGillivray T, MacCormick IJ. Thickness dependent tortuosity estimation for retinal blood vessels. Conf Proc IEEE Eng Med Biol Soc. 2006; 1:4675–8. [PubMed: 17945850]

2. Baatout S. Endothelial differentiation using Matrigel (review). Anticancer Res. 1997; 17:451–5. [PubMed: 9066693]

3. Baluk P, Hashizume H, McDonald DM. Cellular abnormalities of blood vessels as targets in cancer. Curr Opin Genet Dev. 2005; 15:102–11. [PubMed: 15661540]

4. Bauerle T, Komljenovic D, Berger MR, Semmler W. Multi-modal imaging of angiogenesis in a nude rat model of breast cancer bone metastasis using magnetic resonance imaging, volumetric computed tomography and ultrasound. J Vis Exp. 2012:e4178. [PubMed: 22929330]

5. Bian XW, Wang QL, Xiao HL, Wang JM. Tumor microvascular architecture phenotype (t-map) as a new concept for studies of angiogenesis and oncology. J Neurooncol. 2006; 80:211–3. [PubMed: 16708278]

6. Bouxsein ML, Boyd SK, Christiansen BA, Guldberg RE, Jepsen KJ, Muller R. Guidelines for assessment of bone microstructure in rodents using micro-computed tomography. J Bone Miner Res. 2010; 25:1468–86. [PubMed: 20533309]

7. Bullitt E, Gerig G, Pizer SM, Lin W, Aylward SR. Measuring tortuosity of the intracerebral vasculature from MRA images. IEEE Trans Med Imaging. 2003; 22:1163–71. [PubMed: 12956271]

8. Cai W, Chen X. Multimodality molecular imaging of tumor angiogenesis. J Nucl Med. 2008; 49 (Suppl 2):113S–28S. [PubMed: 18523069]

9. Chappell JC, Wiley DM, Bautch VL. How blood vessel networks are made and measured. Cells Tissues Organs. 2012; 195:94–107. [PubMed: 21996655]

10. Costouros NG, Diehn FE, Libutti SK. Molecular imaging of tumor angiogenesis. J Cell Biochem Suppl. 2002; 39:72–8. [PubMed: 12552605]

11. Cuenod CA, Fournier L, Balvay D, Guinebretiere JM. Tumor angiogenesis: Pathophysiology and implications for contrast-enhanced MRI and CT assessment. Abdom Imaging. 2006; 31:188–93. [PubMed: 16447089]

12. Downey CM, Singla AK, Villemaire ML, Buie HR, Boyd SK, Jirik FR. Quantitative ex-vivo micro-computed tomographic imaging of blood vessels and necrotic regions within tumors. PLoS One. 2012; 7:e41685. [PubMed: 22848565]

13. Folarin AA, Konerding MA, Timonen J, Nagl S, Pedley RB. Three-dimensional analysis of tumour vascular corrosion casts using stereoimaging and micro-computed tomography. Microvasc Res. 2010; 80:89–98. [PubMed: 20303995]

14. Fox SB. Assessing tumor angiogenesis in histological samples. Methods Mol Biol. 2009; 467:55–78. [PubMed: 19301664]

15. Fukumura D, Duda DG, Munn LL, Jain RK. Tumor microvasculature and microenvironment: Novel insights through intravital imaging in pre-clinical models. Microcirculation. 2010; 17:206–25. [PubMed: 20374484]

16. Grabherr S, Hess A, Karolczak M, Thali MJ, Friess SD, Kalender WA, Dirnhofer R, Djonov V. Angiofil-mediated visualization of the vascular system by microcomputed tomography: A feasibility study. Microsc Res Tech. 2008; 71:551–6. [PubMed: 18393302]

17. Hegen A, Blois A, Tiron CE, Hellesoy M, Micklem DR, Nor JE, Akslen LA, Lorens JB. Efficient in vivo vascularization of tissue-engineering scaffolds. J Tissue Eng Regen Med. 2011; 5:e52–62. [PubMed: 20865694]

18. Hlatky L, Hahnfeldt P, Folkman J. Clinical application of antiangiogenic therapy: Microvessel density, what it does and doesn't tell us. J Natl Cancer Inst. 2002; 94:883–93. [PubMed: 12072542]

19. Kerbel RS. Tumor angiogenesis. N Engl J Med. 2008; 358:2039–49. [PubMed: 18463380]

20. Kim E, Stamatelos S, Cebulla J, Bhujwalla ZM, Popel AS, Pathak AP. Multiscale imaging and computational modeling of blood flow in the tumor vasculature. Ann Biomed Eng. 2012; 40:2425–41. [PubMed: 22565817]

21. Koh TS, Shi W, Thng CH, Ho JT, Khoo JB, Cheong DL, Lim TC. Assessment of tumor blood flow distribution by dynamic contrast-enhanced CT. IEEE Trans Med Imaging. 2013; 32:1504–14. [PubMed: 23625351]

22. Lang S, Muller B, Dominietto MD, Cattin PC, Zanette I, Weitkamp T, Hieber SE. Three-dimensional quantification of capillary networks in healthy and cancerous tissues of two mice. Microvasc Res. 2012; 84:314–22. [PubMed: 22796313]

23. Langheinrich AC, Ritman EL. Quantitative imaging of microvascular permeability in a rat model of lipopolysaccharide-induced sepsis: Evaluation using cryostatic micro-computed tomography. Invest Radiol. 2006; 41:645–50. [PubMed: 16829748]

24. Lee S, Wurtzel JG, Singhal SS, Awasthi S, Goldfinger LE. RALBP1/RLIP76 depletion in mice suppresses tumor growth by inhibiting tumor neovascularization. Cancer Res. 2012; 72:5165–5173. [PubMed: 22902412]

25. Less JR, Posner MC, Skalak TC, Wolmark N, Jain RK. Geometric resistance and microvascular network architecture of human colorectal carcinoma. Microcirculation. 1997; 4:25–33. [PubMed: 9110281]

26. Less JR, Skalak TC, Sevick EM, Jain RK. Microvascular architecture in a mammary carcinoma: Branching patterns and vessel dimensions. Cancer Res. 1991; 51:265–73. [PubMed: 1988088]

27. Liu P, Li J, Zhang C, Xu LX. Micro-CT molecular imaging of tumor angiogenesis using a magnetite nano-cluster probe. J Biomed Nanotechnol. 2013; 9:1041–9. [PubMed: 23858968]

28. Malinda KM. In vivo matrigel migration and angiogenesis assays. Methods Mol Med. 2001; 46:47–52. [PubMed: 21340910]

29. Marxen M, Thornton MM, Chiarot CB, Klement G, Koprivnikar J, Sled JG, Henkelman RM. MicroCT scanner performance and considerations for vascular specimen imaging. Med Phys. 2004; 31:305–13. [PubMed: 15000616]

30. Minnich B, Lametschwandtner A. Lengths measurements in microvascular corrosion castings: Two-dimensional versus three-dimensional morphometry. Scanning. 2000; 22:173–7. [PubMed: 10888123]

31. Miodonski AJ, Bugajski A, Litwin JA, Piasecki Z. Vascular architecture of human urinary bladder carcinoma: A SEM study of corrosion casts. Virchows Arch. 1998; 433:145–51. [PubMed: 9737792]

32. Norrby K. In vivo models of angiogenesis. J Cell Mol Med. 2006; 10:588–612. [PubMed: 16989723]

33. Ocak I, Baluk P, Barrett T, McDonald DM, Choyke P. The biologic basis of in vivo angiogenesis imaging. Front Biosci. 2007; 12:3601–16. [PubMed: 17485324]

34. Phongkitkarun S, Kobayashi S, Kan Z, Lee TY, Charnsangavej C. Quantification of angiogenesis by functional computed tomography in a Matrigel model in rats. Acad Radiol. 2004; 11:573–82. [PubMed: 15147622]

35. Savai R, Langheinrich AC, Schermuly RT, Pullamsetti SS, Dumitrascu R, Traupe H, Rau WS, Seeger W, Grimminger F, Banat GA. Evaluation of angiogenesis using micro-computed tomography in a xenograft mouse model of lung cancer. Neoplasia. 2009; 11:48–56. [PubMed: 19107231]

36. Schambach SJ, Bag S, Groden C, Schilling L, Brockmann MA. Vascular imaging in small rodents using micro-CT. Methods. 2009; 50:26–35. [PubMed: 19772922]

37. Schoenfeld A, Levavi H, Breslavski D, Amir R, Ovadia J. Three-dimensional modelling of tumor-induced ovarian angiogenesis. Cancer Lett. 1994; 87:79–84. [PubMed: 7525046]

38. Takahashi Y, Akishima-Fukasawa Y, Kobayashi N, Sano T, Kosuge T, Nimura Y, Kanai Y, Hiraoka N. Prognostic value of tumor architecture, tumor-associated vascular characteristics, and expression of angiogenic molecules in pancreatic endocrine tumors. Clin Cancer Res. 2007; 13:187–96. [PubMed: 17200354]

39. Taub M, Wang Y, Szczesny TM, Kleinman HK. Epidermal growth factor or transforming growth factor alpha is required for kidney tubulogenesis in matrigel cultures in serum-free medium. Proc Natl Acad Sci U S A. 1990; 87:4002–6. [PubMed: 2339133]

40. Vegesna AK, Sloan JA, Singh B, Phillips SJ, Braverman AS, Barbe MF, Ruggieri MR Sr, Miller LS. Characterization of the distal esophagus high-pressure zone with manometry, ultrasound and micro-computed tomography. Neurogastroenterol Motil. 2013; 25:53–e6. [PubMed: 22998376]

41. Vukicevic S, Kleinman HK, Luyten FP, Roberts AB, Roche NS, Reddi AH. Identification of multiple active growth factors in basement membrane Matrigel suggests caution in interpretation of cellular activity related to extracellular matrix components. Exp Cell Res. 1992; 202:1–8. [PubMed: 1511725]

PERSPECTIVES

This study establishes a standardized approach to *ex vivo* μCT scanning, reconstruction and measurement of vascular volumes, branch point diameters and angles, segment length distribution, and other architectural parameters, including the microcirculation. By applying a non-biased, thresholded depletion of background X-ray absorbance in scan processing, small diameter vessels can be reconstructed accurately, while eliminating excess voxels from the reconstructions. This allows for precision in quantitation of vascular geometries, which will be particularly valuable in investigations of the unique properties of neovasculature in pathological settings such as in solid tumors. This approach was further used to confirm perfusion in Matrigel plugs, and to measure the vascular parameters in the plugs. Thus, this approach can be utilized for a broad range of studies in macro- and microvascular biology.
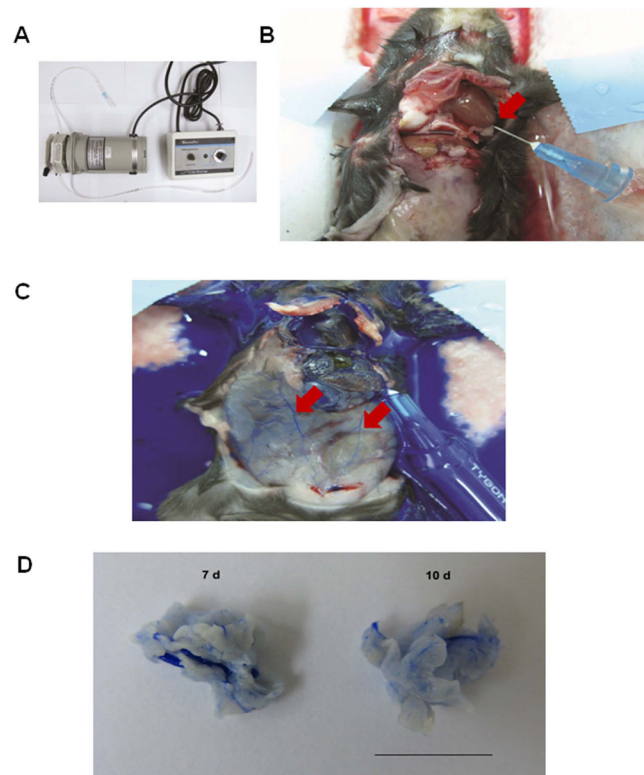
Figure 1. Perfusion of peripheral blood circulation and xenografted tumors with heparin and Microfil

(A) Tubing and pump (pump speed, 2 mL/min). (B) Catherization in left ventricle, for exsanguination with 0.1% heparinized solution. The right atrium is nicked when the catheter is inserted (arrow). (C) Microfil perfusion through the same catheter after heparin treatment. Arrows point to Microfil perfused in peripheral blood vessels. (D) Macroscopic appearance of Microfil-perfused LLC carcinomas derived from a bolus injection of 1×10^6 tumor cells in the mouse flanks at 7 d (left) and 10 d (right). Bar, 10 mm.
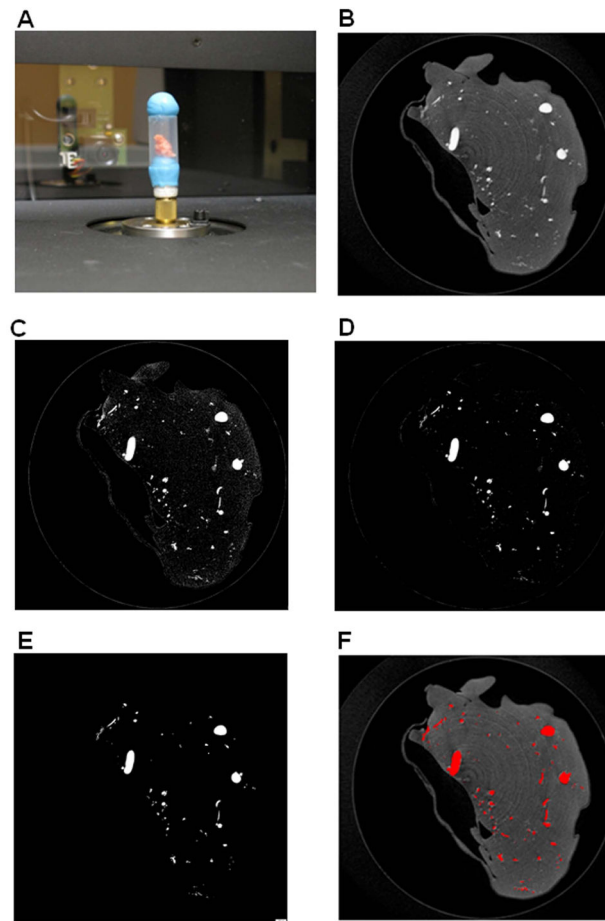
Figure 2. MicroCT scanning set up; raw and thresholded images

(A) A perfused tumor specimen (with orange-colored Microfil solution) prepared for X-ray scanning. The specimen was held in place in a polyethylene tube with poster putty (blue) on top and bottom, and the assembly was fixed onto a brass spigot in the SkyScan scanner. (B) Example of a raw. BMP reconstructed image slice (3 μm thick) from a scanned LLC tumor sample including the polyethylene tube, before reconstruction. Small and large vessels are seen in cross-section as bright grey regions, within the darker grey surrounding tissue, which weakly absorbed the X-rays. The tube, which weakly absorbs X-rays, can usually be seen around the periphery (*). (C) The same cross section from (B) after the first thresholding step (lower limit 75, upper limit 225) using the CTAn Task list. (D) Image from (C) after despeckling. (E) The final cross section converted to a binarised image after a second threshold step (lower limit 105, upper limit 225). This series of steps preserves small diameter vessels, seen here as small white dots, while eliminating background pixels from the surrounding tissue and the tube. (F) Overlay of binarised final image from (E), pseudocolored red, with raw reconstruction scan from (B). Note the absence of background pixels in the final processed image (E), which otherwise can create background voxels in the 3D models that would also be included in the analysis. Bar, 400 μm.
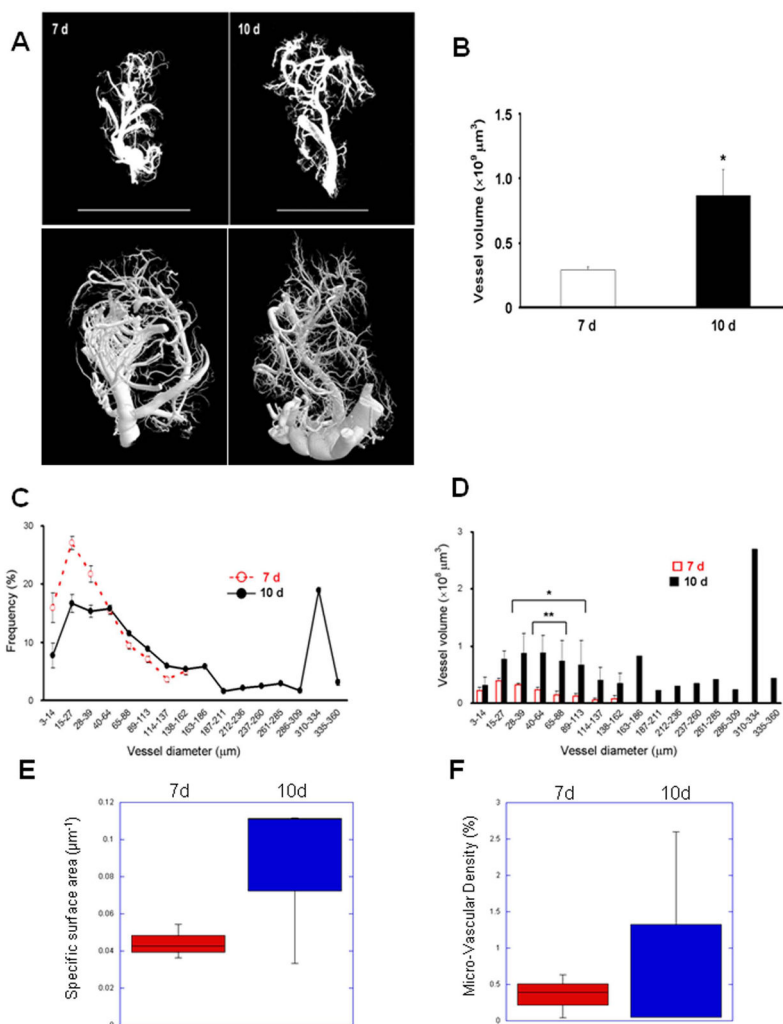
Figure 3. Tumor neovasculature 3D modeling and analysis by X-ray μCT scanning in wild type (WT) C57Bl/6 mice

(A) Sample images of 3D reconstructions of neovasculature in LLC tumors (left, 7 d; right, 10 d) acquired by X-ray μCT scanning of tumors derived as in Figure 1D at 3 μm voxel resolution, followed by post-scan processing and 3D reconstruction. Top row, reconstruction view in CTVol; bottom row, using CTVox (different samples). Bars, 10 mm. (B) Total vessel volumes in 3D reconstructed vascular models from tumors derived in WT mice. n=3, * $p < 0.01$. (C) Frequency distribution of the vascular diameters in LLC tumors at 7 d (dotted red line) and 10 d (solid black line). (D) Individual vessel volumes plotted against vascular diameters from (C) (* $p < 0.05$, ** < 0.01). (E) Vascular specific surface area in 7 d and 10 d tumors determined by the ratio of total vascular surface area to volume. (F) Micro-Vascular Densities in 7 d and 10 d tumors determined as the percentage of total tumor volume occupied by the vascular casts.
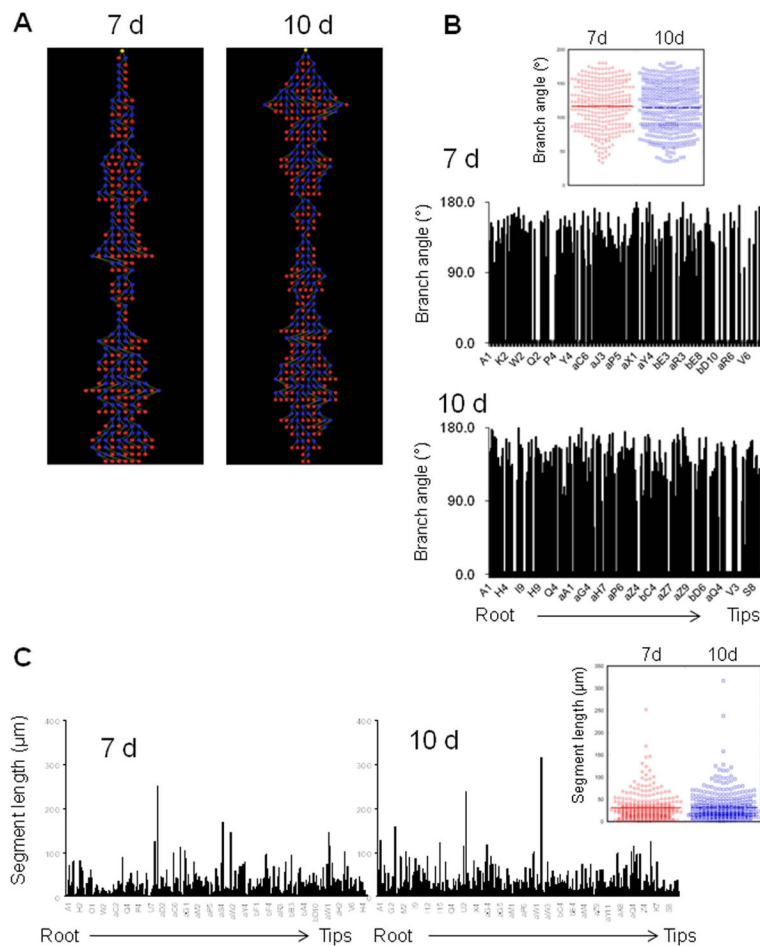
Figure 4. Tree analysis of LLC tumor neovasculature

(A) Representative tree structures determined from μCT vascular reconstructions in xenografted LLC tumors at 7 d (left) and 10 d (right) post-implantation. Yellow nodes represent the tree root, blue nodes indicate branch or bifurcation points, and red nodes indicate branch termini. (B) Branch angle measurements are shown for each tree segment from (A), beginning with "A1" as the root segment. 7 d, top; 10 d, bottom. Inset, dot plot of branch angles at 7 d and 10 d, excluding angles of 0° from non-branched segments. Medians are shown with a horizontal line in each case. (C) Segment length measurements from the tree analysis. 7 d, left; 10 d, right. Inset, dot plot of all segment lengths at 7 d and 10 d. Medians are shown with a horizontal line in each case.
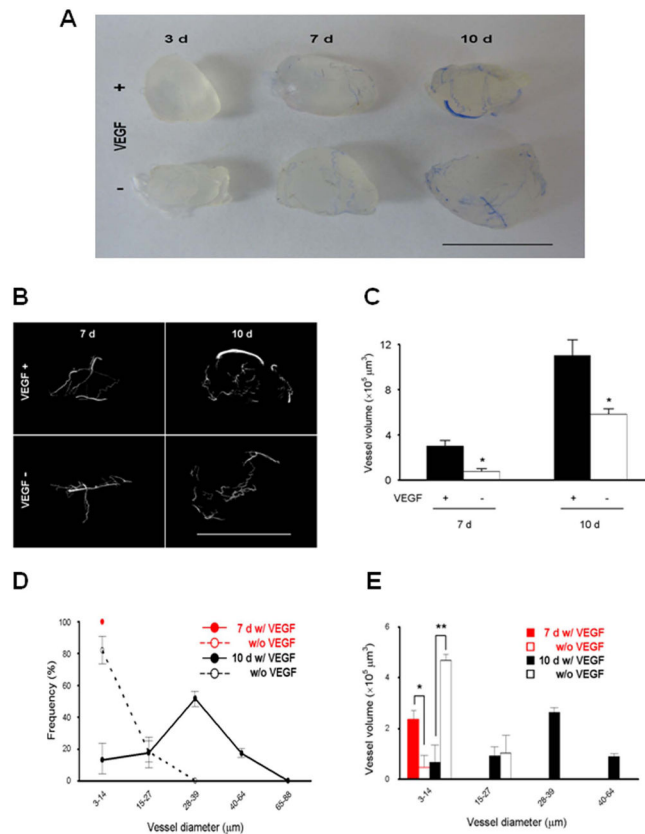
Figure 5. Matrigel plug neovasculature 3D modeling and analysis by X-ray µCT scanning in WT mice

(A) Macroscopic appearance of Matrigel plugs with or without VEGF at 3 d (left), 7 d (middle), and 10 d (right). Bar, 10 mm. (B) Images of 3D models of neovasculature in Matrigel plugs (top, +VEGF; bottom, −VEGF; left, 7 d; right, 10 d) acquired by X-ray µCT scanning at 3 µm voxel resolution and 3D reconstruction. Bar, 10 mm. (C) Total vessel volumes in 3D reconstructed images from Matrigel plugs derived in WT mice. n=3, * $p < 0.001$. (D) Frequency distribution of the vascular diameters in Matrigel plugs at 7 d (red lines) and 10 d (black lines). Dotted lines, −VEGF; solid lines, +VEGF. (E) Individual vessel volumes plotted against vascular diameters in Matrigel plugs from (D) (* $p < 0.001$, ** < 0.0001).

Table 1

Structural comparisons of tumor vasculature at 7 d and 10 d

Total vascular volume, specific surface area (SSA), mean vessel density (MVD), branch angle, segment length, and tortuosity (Tg) are shown ± S.E.M for data compiled from tumor vessels at 7 d and 10 d.

Time	Total vascular Volume ($\times 10^8$ μm^3)	SSA (μm^2)	MVD (%)	Branch angle (°)	Segment length (μm)	Tg (ratio)
7d	2.9 ± 0.78	0.044 ± 0.005	0.35 ± 0.002	116.5 ± 34.5	31.25 ± 1.69	1.25 ± 0.31
10d	8.7 ± 0.6	0.085 ± 0.025	0.90 ± 0.008	114.5 ± 35.5	31.49 ± 1.53	2.63 ± 0.67